BIOMEDICAL ENGINEERING

Material-driven fibronectin assembly for high-efficiency presentation of growth factors

10.1126/sciadv.1600188

Virginia Llopis-Hernández,[1] Marco Cantini,[1] Cristina González-García,[1] Zhe A. Cheng,[1] Jingli Yang,[2] Penelope M Tsimbouri,[2] Andrés J. García,[3]* Matthew J. Dalby,[2]* Manuel Salmerón-Sánchez[1]*

Growth factors (GFs) are powerful signaling molecules with the potential to drive regenerative strategies, including bone repair and vascularization. However, GFs are typically delivered in soluble format at supraphysiological doses because of rapid clearance and limited therapeutic impact. These high doses have serious side effects and are expensive. Although it is well established that GF interactions with extracellular matrix proteins such as fibronectin control GF presentation and activity, a translation-ready approach to unlocking GF potential has not been realized. We demonstrate a simple, robust, and controlled material-based approach to enhance the activity of GFs during tissue healing. The underlying mechanism is based on spontaneous fibrillar organization of fibronectin driven by adsorption onto the polymer poly(ethyl acrylate). Fibrillar fibronectin on this polymer, but not a globular conformation obtained on control polymers, promotes synergistic presentation of integrin-binding sites and bound bone morphogenetic protein 2 (BMP-2), which enhances mesenchymal stem cell osteogenesis in vitro and drives full regeneration of a nonhealing bone defect in vivo at low GF concentrations. This simple and translatable technology could unlock the full regenerative potential of GF therapies while improving safety and cost-effectiveness.

INTRODUCTION

Growth factors (GFs) are potent biological signals that regulate cell growth, stem cell differentiation, and tissue healing (*1*, *2*). GFs are widely used in the clinic despite major problems associated with serious off-target effects due to their required use at supraphysiological levels. These high levels are needed because of the rapid GF breakdown and clearance from target sites. For example, routine clinical delivery of bone morphogenetic protein 2 (BMP-2) in spinal bone fusions involves the incorporation of BMP-2 in a collagen sponge carrier at a concentration of 1.5 mg/ml (*3*). However, serious respiratory, neurological, and inflammatory complications have been reported that eventually led the U.S. Food and Drug Administration to issue a public health notification of life-threatening complications (*4*).

Material-based strategies to direct stem cell–based tissue repair focus mostly on controlling integrin adhesion receptor–related signaling through alterations in surface chemistry, stiffness, and nanotopography (*5*–*12*). These approaches have provided marked results, most notably in the area of bone cell, osteoblast, and differentiation. However, these materials are highly engineered, nonbiocompatible, or very delicate, and thus, translation remains a hurdle. Furthermore, these material-based approaches typically do not control GF binding and activity. Therefore, materials that mimic and exploit GF interactions with extracellular matrix (ECM) proteins such as fibronectin (FN) may provide novel substrates for localized, low-dose delivery with high potency (*1*).

Seminal work has demonstrated that FN contains domains for effective GF binding (*13*). However, when adsorbed onto synthetic materials, FN typically adopts a globular conformation that is suboptimal for presentation of GF- and integrin-binding regions (*13*, *14*). Alternatively, engineered recombinant proteins including integrin-binding and GF-sequestering domains from FN have been incorporated within a fibrin matrix to bind BMP-2 and promote bone repair (*15*). However, this strategy relies on recombinant protein technology of a fibrin matrix and intricate engineering that increases costs and complexity (*16*, *17*). Other approaches used to increase the effect of GFs by presenting them within material systems [for example, using biopolymers based on polyelectrolyte multilayers (*18*), heparin-binding peptides that sequester cell-secreted heparin proteoglycans and GFs (*19*), and mineral coatings used as templates that bind GFs (*20*, *21*)] are being explored, but these strategies typically involve high GF doses.

Here, we demonstrate a simple, robust, and translational approach to present BMP-2 in synergy with the integrin-binding domain of FN. To achieve this, we use a simple polymer coating that spontaneously assembles FN molecules into biological networks (*22*). Processing of the synthetic polymers to produce our coatings involves solvents, but these are removed after the fabrication process (spin coating), and it is envisaged that we can use non–solvent-based techniques such as plasma polymerization. Here, we show that this material-driven FN fibrillogenesis provides synergistic integrin/BMP-2 signaling that drives osteoblastic differentiation in primary human mesenchymal stem cells (MSCs) in vitro and fully repairs nonhealing bone defects in vivo. It is critical to note that this is achieved at a ~300-fold lower GF dose than with collagen sponge delivery.

RESULTS

Material-driven FN networks facilitate GF binding with enhanced activity

Plasma FN is a dimeric glycoprotein with two subunits (~220 kD) linked by a single disulfide bond. Each subunit contains three types

---

[1]Division of Biomedical Engineering, School of Engineering, University of Glasgow, Glasgow G12 8LT, UK. [2]Center for Cell Engineering, Institute of Molecular Cell and Systems Biology, University of Glasgow, Joseph Black Building, University Avenue, Glasgow G12 8QQ, UK. [3]Woodruff School of Mechanical Engineering, Petit Institute for Bioengineering and Bioscience, Georgia Institute of Technology, 315 First Drive, Atlanta, GA 30332, USA.
*Corresponding author. Email: manuel.salmeron-sanchez@glasgow.ac.uk. (M.S.-S.); matthew.dalby@glasgow.ac.uk. (M.J.D.); andres.garcia@me.gatech.edu. (A.J.G.)

of repeating modules (types I, II, and III), which mediate interactions with other FN molecules (FNI_{1-5} and $FNIII_{1-2}$), other ECM components, integrins ($FNIII_{9-10}$), and GFs ($FNIII_{12-14}$) (Fig. 1A) (*23*). Cells primarily interact with FN via integrins, a family of transmembrane cell adhesion receptors. Integrin-mediated adhesion is a complex process that involves clustering into supramolecular complexes that contain signaling molecules and association with the actin cytoskeleton (*24*). We have previously shown that adsorption of individual FN molecules onto a particular surface chemistry [poly(ethyl acrylate) (PEA)] induces exposure of self-assembly sites (FNI_{1-5}) to drive FN assembly at the material interface (Fig. 1B) (*25*). This process involves the 70-kD N-terminal fragment of FN, which is required in physiological, cell-induced, FN fibrillogenesis (*26*), giving rise to material-driven FN fibrillogenesis (Fig. 1B) (*22*). Poly(methyl acrylate) (PMA) is used as a reference polymer on which FN is adsorbed and maintains a globular conformation (Fig. 1B). PMA otherwise behaves similarly to PEA in

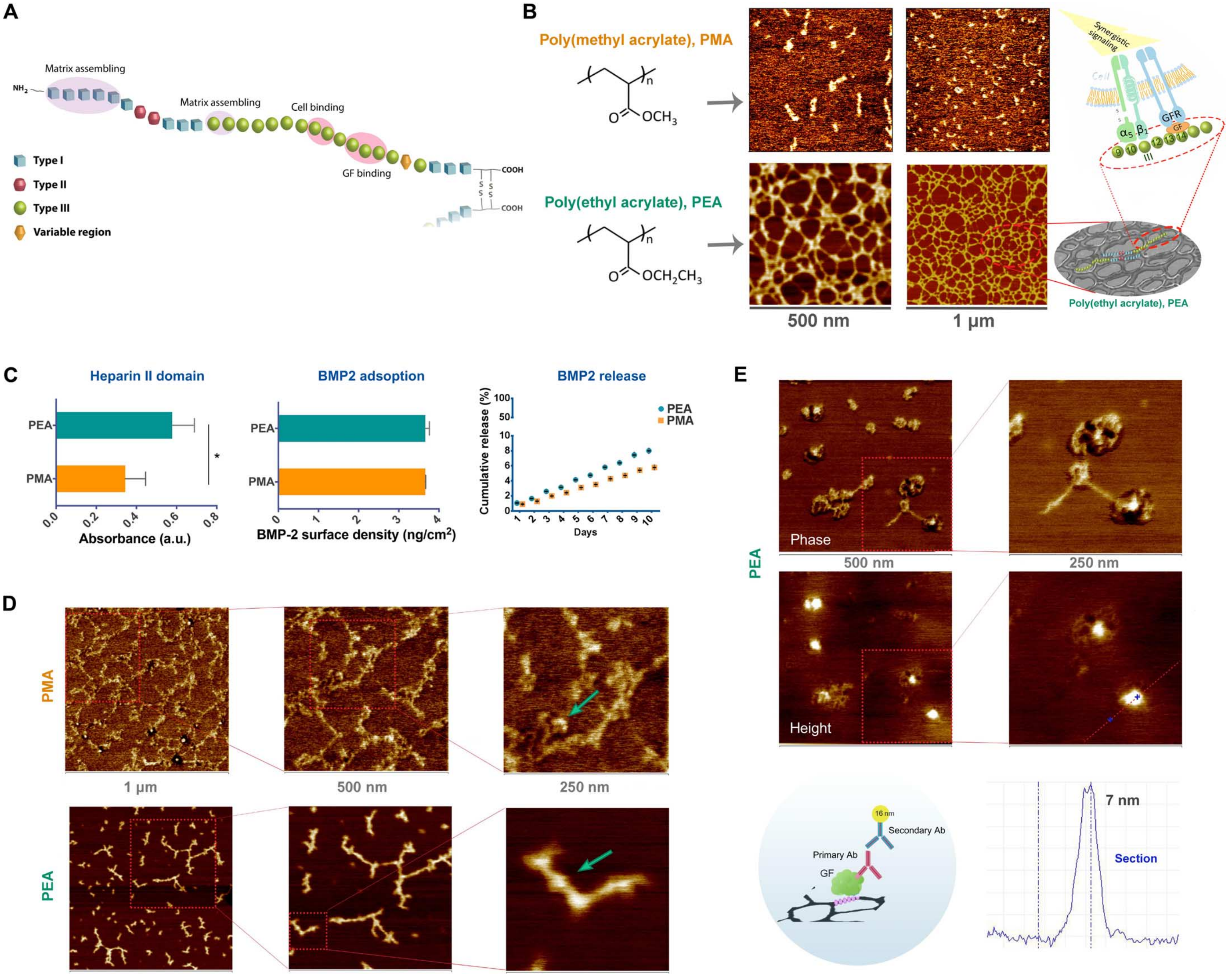

Fig. 1. Fibril-based GF presentation. (**A**) FN contains three types of domains that promote integrin binding (III_{9-10}), GF sequestration (III_{12-14}), and FN-FN interactions (I_{1-5}). (**B**) FN adsorption results in an FN nanonetwork spontaneously assembled on the material surface of PEA but not on PMA, allowing us to propose synergistic integrin/GF receptor signaling to direct MSC differentiation in vitro and tissue healing in vivo. (**C**) FN organized into fibrils on PEA displays higher availability of the GF-binding region ($FNIII_{12-14}$) than FN adsorbed on PMA in a globular conformation (left). However, similar surface density of BMP-2 on FN-coated PEA and PMA occurs regardless of the organization and conformation of FN on both surfaces (center). Very low release of BMP-2 over 14 days was observed using enzyme-linked immunosorbent assay (ELISA). (**D**) Atomic force microscopy (AFM) images at different magnifications after the sequential adsorption of FN (3 μg/ml) and BMP-2 (25 ng/ml) on PEA and PMA. No FN/BMP-2 interactions were noted on PMA (only random apposition of both molecules on the surface), whereas on PEA fibrillar FN molecules contained globular aggregates that we proposed to be BMP-2. (**E**) AFM images of BMP-2 interacting with single FN molecules on PEA (top, phase magnitude; bottom, height magnitude as indicated on the pictures), where a secondary antibody (Ab) bound to a 15-nm gold nanoparticle was used to identify BMP-2 on FN. The Tukey-Kramer method was used with multiple-comparisons posttest analysis of variance (ANOVA). Symbols show statistical significant differences with all the other conditions on PEA (*P 0.001). a.u., arbitrary unit.

terms of surface wettability, stiffness, and total surface density of adsorbed FN (*22*). We have previously shown that this phenomenon of organization of FN on PEA depends on the concentration of the solution from which FN adsorption takes place, and a minimum concentration of >10 μg/ml is needed to achieve a full interconnection of FN on PEA; increasing the concentration of FN on PMA only results in a higher density of globular molecules on the surface (*27*). In addition, the phenomenon is rapid and allows FN organization within a time scale of ~1 min (*28*). Further, we have recently shown that the combination of EA and MA in a random copolymer modulates the interconnection of FN nanonetworks in dependence of the composition of the system (*29*).

Antibody-based assays revealed that FN was adsorbed on PEA in a conformation that favors the simultaneous availability of the GF-binding domain ($FNIII_{12-14}$) next to the integrin-binding region ($FNIII_{9-10}$) (Fig. 1C, left) (*30*). Note that this change in the structure of FN occurs without the application of external force, a method known to alter the exposure of cryptic type III domains (*31*). The total surface density of BMP-2 on these two FN-coated surfaces, quantified by ELISA, was similar for PEA and PMA (Fig. 1C, center), and BMP-2 remained stably adsorbed on these surfaces as a function of time, with less than 10% released after 14 days (Fig. 1C, right).

AFM examination showed that BMP-2 was preferentially adsorbed on top of FN molecules on PEA, whereas on PMA the GF appeared adsorbed over the polymer surface (Fig. 1D). Bare PEA and PMA surfaces are shown in fig. S1, and BMP-2 molecules directly adsorbed on PEA and PMA (without FN) are shown as individual globules in fig. S2. Figure 1D includes molecular-scale AFM phase magnitude images of individual BMP-2 molecules sequestered onto open FN dimers (*32*). The FN open conformation sequestration of BMP-2 molecules was assessed using an anti–BMP-2 antibody and then a secondary antibody labeled with a gold nanoparticle (Fig. 1E). Individual FN molecules on PEA were observed using phase magnitude, whereas the gold nanoparticles were depicted using height magnitude. A high-resolution AFM image of one of these FN molecules in an extended conformation adsorbed on PEA with one gold nanoparticle per FN arm is shown in Fig. 1E; the section shows a height profile of ~7 nm that is compatible with the dimensions of the gold nanoparticles buried within the antibody cluster. These results demonstrate that FN adsorption onto PEA, but not PMA, results in controlled binding and presentation of BMP-2 to the adsorbed FN molecules.

Synergistic integrin/GF signaling drives MSC osteogenesis

To test whether PEA-driven integrin/BMP-2 presentation drives MSCs to osteoblast differentiation through a synergistic mechanism, BMP-2 (25 ng/ml) was adsorbed onto FN-coated PEA surfaces. The ability of the PEA-controlled FN presentation to drive paired integrin and BMP receptor localization required to drive synergistic signaling was examined using coimmunoprecipitation of integrin β_1, which forms part of the FN receptor (*33*), and the BMP-2 receptor, BMPRIa. Colocalization was seen using an anti-BMPRIa antibody in denaturing conditions as a band at 60 kD (Fig. 2A) and quantified using the condition without BMP-2 as a reference. These receptor coassemblies were reduced either on FN nanonetworks assembled on PEA without any BMP-2 or if the GF-binding site of FN ($FNIII_{12-14}$) had been previously blocked with a monoclonal antibody (P5F3) to prevent BMP-2 binding (Fig. 2A, left). This colocalization of integrin and GF receptors could also be seen at an individual cell level using immunofluorescence (Fig. 2A, right). Figure S3 shows that colocalization is specific to integrin β_1 and does not happen with integrin β_5, another potential FN receptor (*23*).

This receptor colocalization had clear effects on subsequent cell signaling. We first examined mediators of canonical BMP-2 signaling, the Smads (small mothers against decapentaplegic), after 45 min of MSC adhesion. Smads 1, 5, and 8 are phosphorylated by BMPRIa and then translocate into the nucleus to activate RUNX2 (runt-related transcription factor 2; the osteogenic master transcription factor) (*34*). Results showed that Smads 1 and 5 were significantly more phosphorylated in the active state, with synergistic BMP-2 presentation on PEA (Fig. 2B). Blocking the GF-binding region of FN ($FNIII_{12-14}$) with the P5F3 antibody or adding no BMP-2 reversed pSmad 1 and 5 phosphorylation to control levels, confirming that enhanced Smad signaling is due to synergistic BMP-2 presentation. To confirm this, imaging of Smads 1 and 5 (after 90 min of MSC adhesion) showed arge up-regulation when BMP-2 was synergistically presented (Fig. 2D).

We next examined the phosphorylation of ERK 1/2 that is implicated in noncanonical BMP signaling; we note that this is complicated because ERK 1/2 is also involved in focal adhesion signaling (*35*, *36*). Phospho-ERK (pERK) 1/2 levels were significantly higher for MSCs cultured on FN fibrils with BMP-2 sequestered and had increased trend for MSCs exposed to BMP-2 as a soluble factor in the culture medium at 25 ng/ml compared to no BMP-2 control (Fig. 2C). This allows a number of hypotheses to be proposed—that ERK 1/2 is activated by noncanonical BMP-2 signaling, adhesion-related signaling, or both pathways. Imaging showed that focal adhesion kinase (FAK) expression, which would drive ERK 1/2 phosphorylation in adhesion-related signaling pathways, was unchanged for all conditions [Fig. 2D; expression of phospho-FAK (pFAK) was negligible at this time point as shown in fig. S4]. Again, pERK 1/2 expression was elevated with both adsorbed and soluble BMP-2 (Fig. 2D), allowing us to propose noncanonical BMP-2 activation of ERK 1/2. We note that previous work has shown that there is no difference in adhesion size in MSCs on PMA or PEA with FN adsorbed, again supporting that the observed changes are driven by BMP-2 (*37*).

These results support the conclusion that enhanced canonical BMP-2 signaling is a consequence of the simultaneous occupancy of integrins and BMP-2 receptors (*34*). Furthermore, the data suggest that this synergy is mediated by ERK 1/2 via a lesser degree of noncanonical BMP signaling and that this ERK 1/2 mechanism may be more promiscuous to both synergistic and soluble BMP-2 administration (Fig. 2E).

We next evaluated whether synergistic interactions between FN and BMP-2 when immobilized on PEA modulate MSC osteogenesis. We have noted that Smads and ERK 1/2 act to regulate RUNX2, and Fig. 2D shows enhanced active phospho-RUNX2 (pRUNX2) expression in MSCs cultured on the synergistically presented BMP-2 environments compared to cultures using P5F3 or soluble BMP-2. These differences in pRUNX2 may result in downstream effects on the expression of osteogenic proteins regulated by RUNX2 (*38*). qPCR results for osteogenic markers and the corresponding immunofluorescence images were measured after 14 days of MSC culture to capture early stages of cell differentiation. Figure 2 shows that synergistic integrin/BMP-2 presentation driven by PEA led to significantly higher osteocalcin and osteonectin expression at the transcription and protein levels (Fig. 2, F and G). This system was significantly more effective than soluble administration of the GF (BMP-2 medium; Fig. 2F). Also, when the same experiments were done using PMA, where FN was adsorbed in a globular conformation, the level of cell differentiation was low and insensitive to the route used to present the GF (Fig. 2F). These results indicate that the presentation of BMP-2 in synergy with the adhesion sites on FN on PEA is more effective at triggering MSC osteoblastic differentiation compared to both the same concentration of the GF on PMA and the soluble administration of the GF. Figure 2H shows that bone-related ALP activity was higher when BMP-2 was presented bound on FN on PEA compared to the soluble administration. Figure 2H further demonstrates that blocking of BMP-2 with noggin reduced PEA-driven FN/BMP-2 osteogenic differentiation, further implicating BMP-2 signaling.

Synergistic presentation of BMP-2 on material-driven FN networks drives bone regeneration in a nonhealing defect

We evaluated the potential of the synergistic presentation of GFs and adhesion sites on biomaterials in vivo using a murine nonhealing radial bone defect model (*39*). This bone repair model has significant advantages: (i) the 2.5-mm defect does not spontaneously heal, providing

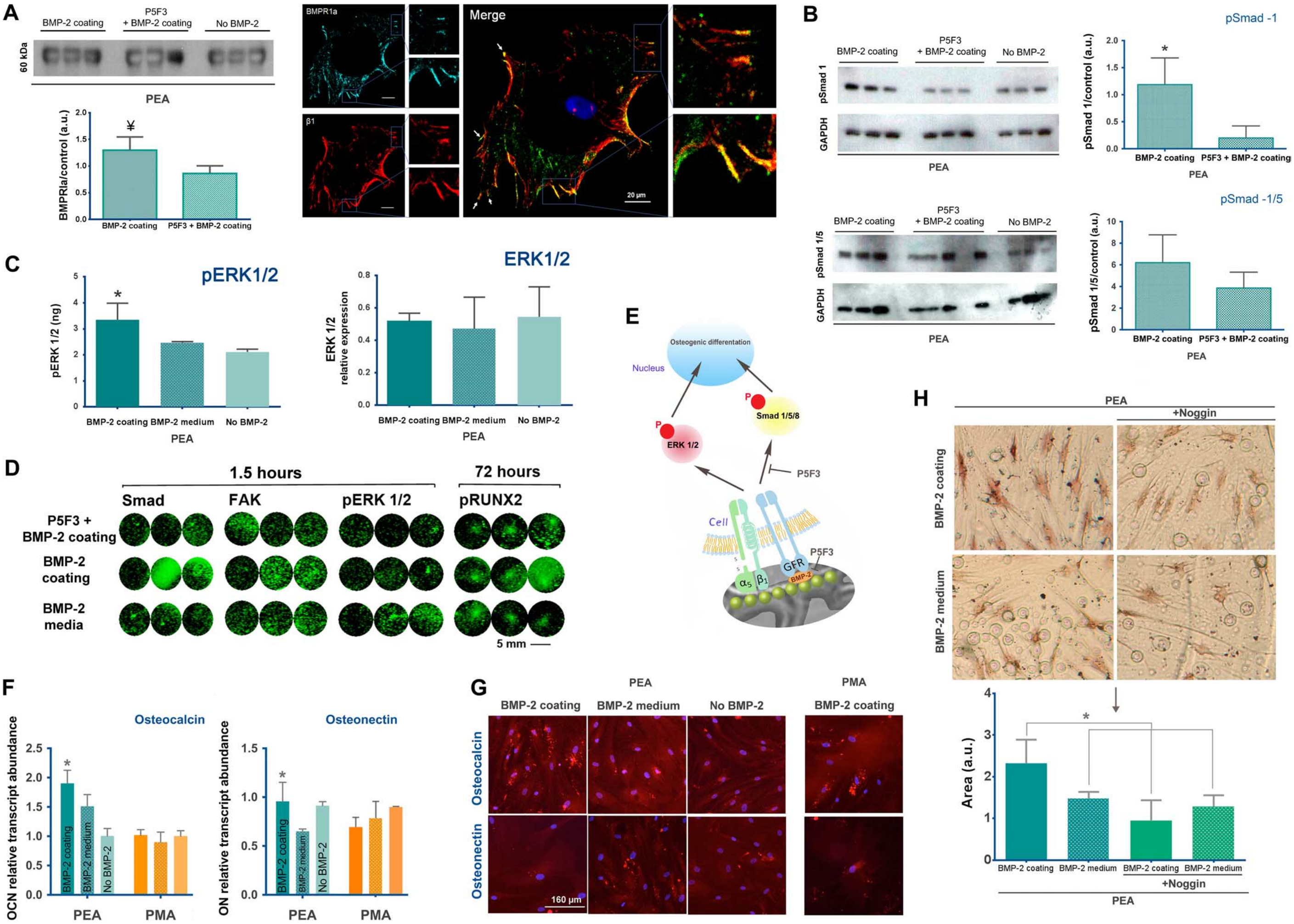

Fig. 2. Integrin/BMP-2 receptor cosignaling drives MSC osteogenesis. (**A**) Coimmunoprecipitation of integrin β_1 and BMPRI occurred on BMP-2 sequestered by FN on PEA, and bands correspond to BMPRIa (60 kD) after precipitation with anti–integrin β_1 antibodies. The graphs show quantification of bands relative to the absence of BMP-2. This colocalization can also be seen in individual cells with integrin β_1 (stained red) and BMPRIa (stained green). (**B**) Smad signaling was drastically altered when BMP-2 was presented bound on $FNIII_{12–14}$; blocking this GF-binding domain of FN (using the monoclonal antibody P5F3 at a molar ratio of 1 with FN to block the GF-binding site) reduces Smad signaling. GAPDH, glyceraldehyde-3-phosphate dehydrogenase. (**C**) Phosphorylation of extracellular signal–related kinase (ERK) 1/2 was significantly enhanced on PEA when BMP-2 was presented at the material interface, sequestered on FN, compared to the presence of the same doses of the soluble factor. (**D**) In-cell Western assay for Smad, FAK, pERK 1/2, and pRUNX2 with BMP-2 on FN on PEA, soluble BMP-2, and blocking with P5F3 before BMP-2 adsorption. (**E**) This fulfills the first part of the synergistic signaling hypothesis. (**F**) Quantitative polymerase chain reaction (qPCR) for osteocalcin (OCN) and osteonectin (ON) after 14 days of culture (PEA and PMA); enhanced expression occurs when BMP-2 was presented bound on FN compared to soluble administration of the GF or when BMP-2 was sequestered on the material surface (PMA) but not bound to FN. (**G**) Immunofluorescence for osteocalcin and osteonectin confirmed the results obtained at the gene level [red, osteocalcin/osteonectin; blue, 4′,6-diamidino-2-phenylindole (DAPI)]. (**H**) Alkaline phosphatase (ALP) staining on PEA comparing BMP-2 bound to FN fibrils versus soluble BMP-2. Noggin (50 ng/ml) was used in both conditions as the BMP-2 inhibitor to prevent activity (image quantification included in the graph). Results show means ± SD [*n* = 3 for all experiments, except for the graph in (H), where 9 images were used]. The Tukey-Kramer method was used with multiple-comparisons posttest ANOVA. Symbols show statistical significant differences with all the other conditions ($^*P = 0.001$, $^¥P = 0.01$).

a rigorous critical-size model; (ii) it allows for simple in vivo imaging approaches [for example, Faxitron and microcomputed tomography (μCT)]; and (iii) the ulna provides sufficient stabilization of the defect, and no fixation plates and hardware are required, thereby simplifying the surgical procedure and reducing the risk of infection, a major advantage over the rat calvaria and segmental femur defect models (*39*).

The implant consisted of polyimide sleeves (4 mm long; Fig. 3A) coated with a thin layer of the PEA and PMA polymers (green fluorescent dye in Fig. 3A). Then, either FN or FN/BMP-2 was adsorbed on the cylindrical polymer surface. We used a very low concentration of BMP-2, which resulted in ~15 ng of BMP-2 on the wall of the coated tubes (surface density of 100 ± 8 ng/cm^2, as measured using ELISA). This BMP-2 amount is still at least 50% lower than most advanced materials systems that have been tested in murine models based on integrin-specific polyethylene glycol (PEG) hydrogels loaded with BMP-2 (*39*). Note that even if humans and rodents do not metabolize biologics at the same rate, the amount of BMP-2 we used is ~300-fold lower than the clinical standard (*3*). The material system is highly demanding because we intend to promote bone regeneration of a nonhealing defect—a volumetric defect—by engineering

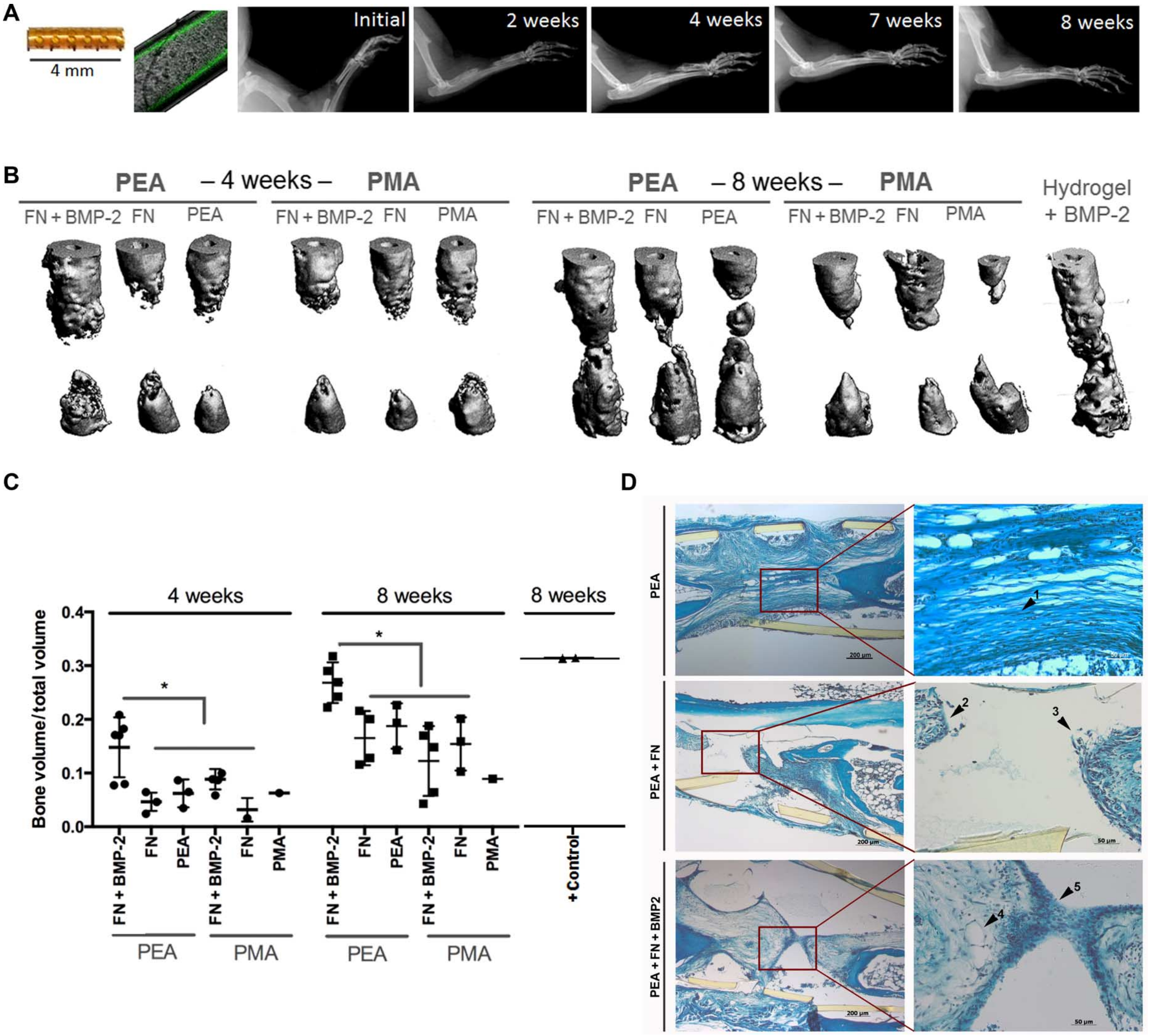

Fig. 3. Bone regeneration in a critical-size defect with very low doses of BMP-2. (**A**) A cylindric polyimide sleeve was coated with the polymers (either PEA or PMA; the figure shows a picture of the sleeve and the coating is shown with a florescent dye) and implanted in a critical-size defect (2.5 mm) in a murine radius. Faxitron images show the evolution of the defect at different time points after implanting PEA coated with FN and BMP-2. The total amount of BMP-2 was ~15 ng. (**B**) Three-dimensional (3D) μCT reconstructions for both PEA and PMA polymers after 4 and 8 weeks, with three conditions: polymer only (PEA and PMA), FN coating on the polymer (FN), and FN coating on the polymer followed by BMP-2 adsorption (FN + BMP-2). The positive control is a PEG hydrogel loaded with ~175 ng of BMP-2. (**C**) μCT measures of bone volume within the defects. (**D**) Sections of 8-week radial samples stained with Safranin O/Fast Green. Arrow 1 shows the fibroblast-like morphology of cells. Arrows 2 and 3 show the new bone cells coming out of both distal and proximal sides. Arrow 4 shows bone marrow–like cavities found in the new bone. Arrow 5 shows the point at the contact point of new bone, coming out of both distal and proximal sides. Five animals (*n* = 5) per condition were used. Symbols show statistical significant differences with all the other conditions (*P = 0.001).

the material surface of a tube where this volume is contained. This is fundamentally different from what has been done to date to promote bone formation in vivo using engineered space-filling materials such as hydrogels and porous scaffolds (*39*). We have included a PEG hydrogel loaded with BMP-2 (75 μg/ml; ~175 ng within the defect) as a positive control in Fig. 3. This represents more than 100 times the amount used in our system to achieve a similar quantitative result (Fig. 3C).

We evaluated bone healing by radiography and μCT at 4 and 8 weeks after implantation (Fig. 3, A and B). We examined three groups for each of the coatings (PEA and PMA): (i) polymer only, (ii) polymer coated with FN (20 μg/ml), and (iii) polymer coated with FN and BMP-2 (~15 ng). Results for μCT, including quantification of bone volume (Fig. 3C), show that only when FN and BMP-2 were adsorbed on PEA did the defect become fully repaired and bridged. Thus, the effect could only be ascribed to the simultaneous presence of FN and BMP-2, promoting enhanced activity of the GF. The sleeve coated with either PEA only or PEA + FN did not promote the same level of bone growth, although FN did have some effect by itself with PEA (Fig. 3B). Also, this very low amount of BMP-2 was not effective in promoting bone growth when presented on PMA surfaces with FN (Fig. 3B). This result supports the specificity of the synergistic integrin/GF receptor mechanism on PEA shown in Fig. 2. Histological analysis at 8 weeks showed fibrous tissue with no significant bone formation within the defect for all the conditions except for PEA + FN + BMP-2, where bone formation and bone marrow establishment in the center of the defect were noted (fig. S5). Higher-magnification images within the defect confirm different tissue architecture among PEA, PEA + FN, and PEA + FN + BMP-2 (Fig. 3D). Without BMP-2, cells are organized along a fibrillar ECM with a fibroblastic morphology. However, on PEA + FN + BMP-2, cells are organized into cavity-like structures as in the bone marrow (arrows in Fig. 3D). There is also a lack of bone marrow–related structures in the cell organization observed on PEA+ FN (arrows).

DISCUSSION

The critical importance of protein structure in determining cell behavior is known (*40*–*42*), but translating this strategy into clinically relevant therapies has been challenging. Here, we describe a facile yet robust engineering approach that allows reliable control of synergistic integrin/GF signaling to promote stem cell differentiation and tissue repair. Notably, PEA can be readily applied to diverse biomedical devices, both planar and complex 3D geometries by spin coating, solvent casting, and plasma polymerization (*43*). We demonstrate that FN nanonetworks, simply adsorbed onto PEA from a solution, allow for simultaneous availability of the integrin-binding region (FNIII_{9-10}) and the GF-binding region (FNIII_{12-13}) (*44*) of this important ECM protein. The FNIII_{12-14} region is classically described as the heparin-binding region shown to be a promiscuous GF-binding region able to sequester different GF families [for example, platelet-derived growth factor (PDGF), fibroblast growth factor (FGF), and transforming growth factor–β (TGF-β)] (*13*). As a proof of concept, we show here that BMP-2 is bound onto the FN nanonetworks at the material interface, and this binding/presentation promotes enhanced BMP-2 signaling in MSCs, with very low doses of BMP-2 driving osteogenesis and complete repair of nonhealing defects in vivo. We show, for the first time, a surface-induced regeneration of the bone (volume) in a critical-size defect, emphasizing clinical potential. Previous studies have shown the importance of FN conformation in driving osteogenic differentiation on material surfaces, with correct FN conformation required to allow enhanced availability of the integrin-binding site (*41*). Coating implants with FN fragments leads to better osteointegration, which reveals the importance of integrin specificity–related mechanisms also in vivo (*45*). Our results show a moderate effect for fibrillar FN nanonetwork presentation on PEA to induce osteogenesis both in vitro, as previously reported (*37*), and in vivo (Fig. 3). This may be related to the presence of GFs in the regenerative environment (medium/serum), which are adsorbed on FN nanonetworks to induce synergistic signaling.

Other strategies to present GFs from a material surface, including protein engineering techniques, the use of peptides that bind heparin and then GFs (*19*), and the use of layer-by-layer technologies (*16*, *18*), have been shown to be more effective than the soluble administration of GFs but, critically, do not exploit synergy between GF and integrin receptors to accelerate healing (*1*). The potential importance of crosstalk between integrins and GFs was revealed in biological sciences more than a decade ago (*46*) and was explicitly engineered into a fibrin matrix using a recombinant fragment of FN consisting of $\text{FNIII}_{9-10}/\text{FNIII}_{12-14}$ that promoted bone regeneration and wound healing (*15*). More recently, it has been shown that matrix-bound BMP-2 induced integrin-dependent Smad signaling, which helped indicate that both receptors in synergy can potentiate each other to increase control over cell fate (*47*). Note that this work only presented BMP-2 from the material surface, and it was hypothesized that cell-secreted FN was used to promote receptor crosstalk and simultaneous integrin BMP receptor signaling. However, we have engineered the cellular microenvironment to synergistically target integrins and GF receptors with facile and translatable materials technology.

Currently, although widely used in the clinic (for example, bone repair), the use of GFs has only been partially successful and even controversial. Our polymer system has the potential to drastically reduce GF dose and topically deliver the GFs to the site of regenerative demand, maximizing the effects by targeting integrins and GF receptors in synergy. Furthermore, the GFs remain bound and localized to the material, and therefore, off-target effects should be reduced.

MATERIALS AND METHODS

Preparation of materials and synergistic interfaces

Polymer sheets were obtained by radical polymerization of a solution of the corresponding alkyl acrylate, that is, MA (methyl acrylate) and EA (ethyl acrylate) (Sigma-Aldrich), using 1 and 0.35 weight percent benzoin, respectively (98% pure; Scharlau), as a photoinitiator. The polymerization was carried out up to limiting conversion. After polymerization, low–molecular mass substances were extracted from the material by drying in vacuo to constant weight. Thin films were prepared by using a spin coater (Brewer Science). To do that, PMA and PEA were dissolved in toluene at a concentration of 6 and 2.5%. Spin casting was performed on glass coverslips at 2000 rpm for 30 s. Samples were dried in vacuo at 60°C before their use. FN from human plasma (Sigma) was adsorbed from solutions of 20 μg/ml for 1 hour at room temperature (RT) and blocked in 1% bovine serum albumin (BSA) (Sigma)/Dulbecco's phosphate-buffered saline (DPBS) for 30 min at RT. For GF adsorption, BMP-2 (25 ng/ml; R&D Systems, 355-BM or 355-BM/CF for AFM studies) in DPBS was used for 1 hour at RT. For AFM studies, FN was adsorbed from solutions of 3 μg/ml in DPBS. To observe the sole GF on the surface, 100 ng/ml was used as the concentration of BMP-2. For synergy-blocking assays, FNIII_{12-14} domains were blocked before BMP-2 coating using the monoclonal P5F3 antibody against this specific region (Santa Cruz Biotechnology, sc-18827; 15 μg/ml). Finally, samples were rinsed in DPBS to eliminate the nonadsorbed protein.

Atomic force microscopy

Experiments were performed using a multimode AFM equipped with a NanoScope IIIA controller (Bruker) operating in tapping mode; the NanoScope 5.30r2 software version was used. Si cantilevers (Bruker) were used with a force constant of 2.8 N/m and a resonance frequency of 75 kHz. The phase signal was set to 0 at a frequency 5 to 10% lower than the resonance one. Drive amplitude was 600 mV, and the amplitude set point A_{sp} was 1.8 V. The ratio between the amplitude set point and the free amplitude (A_{sp}/A_0) was kept equal to 0.8.

Immunogold staining

We used fixed samples (4% formaldehyde, 30 min at RT) with the different protein-coating conditions. Samples were incubated with an anti–BMP-2/BMP-4 antibody (Santa Cruz Biotechnology, sc-9003; 1 hour at RT). After the samples were washed three times with DPBS/0.5% Tween 20 in agitation, they were incubated with 15-nm gold particle–conjugated anti-rabbit immunoglobulin G (IgG) (Aurion, 815.011; 1 hour at RT). Finally, the samples were washed and fixed (2% glutaraldehyde; 5 min at RT).

Availability of the FNIII_{12-14} domain

After coating with FN, a monoclonal antibody for the FNIII_{12-14} domain (also known as heparin II domain) was used (Santa Cruz Biotechnology, sc-18827; 1:30, 2 hours at 37°C). Samples were washed three times with DPBS/0.5% Tween 20. An anti-mouse IgG horseradish peroxidase–conjugated antibody (Invitrogen, 626520; 1:2000, 1 hour at RT) was then used. After the samples were washed twice, they were exposed to the substrate solution (R&D Systems, DY999) and incubated for 20 min at RT in the dark. A stop solution (R&D Systems, DY994) was added before the absorbance was read at 450 nm.

Quantification of BMP-2 adsorption

Both on bare or FN-coated surfaces, the amount of nonadsorbed GF that remained in the supernatant was measured via a sandwich ELISA (R&D Systems, DY355) following the manufacturer's instructions. The standard curve was calculated using a 4PL curve fit (Prism). For stability studies, the release of the BMP-2 was measured at 10 different time points (2 hours and 1, 2, 3, 4, 5, 6, 7, 11, and 14 days) using the same sandwich ELISA.

Cell culture

Human bone marrow MSCs from PromoCell were maintained in basal medium [α-minimum essential medium, 10% fetal bovine serum (FBS), 1% penicillin/streptomycin, 1% fungizone, 2 mM L-glutamine, FGF-2 (1 ng/ml)] at 37°C with 5% CO_2. Cells ($10^4/cm^2$) were seeded onto the materials using the seeding medium (high-glucose Dulbecco's modified Eagle's medium, 1% penicillin/streptomycin, 1% FBS), and the medium was changed twice a week. For all cultures, the first 2 hours (initial cell adhesion) were in the absence of serum and GF. Cells were used at passages P0 to P3. Each experiment was performed in triplicate.

Coimmunoprecipitation

After 45 min of cell culture, cell lysates [radioimmunoprecipitation assay (RIPA) buffer] were used to perform immunoprecipitation of integrin β_1 and the BMP-2 receptor BMPRIa. Proteins (15 μg) were measured using NanoDrop (Thermo Fisher Scientific). First, an integrin β_1 antibody (Abcam, 183666; 10 μl per reaction) was used together with Protein A-Agarose beads (Santa Cruz Biotechnology, sc-2001). Second, after denaturation and elution of beads, the samples were run in NuPAGE 4-12% bis-tris gels (Life Technologies). A mouse BMPRIa antibody was used to probe the membrane (Abcam, 166707; 1:1000). An anti-mouse secondary antibody was used (Santa Cruz Biotechnology, sc-2031; 1:5000). The enhanced chemiluminescence detection system (GE Healthcare) was used before the blot was exposed to x-ray.

ERK 1/2 phosphorylation

ERK 1/2 phosphorylation was quantified using phospho-ELISA kits. Briefly, ELISA plates were coated with a capture antibody for ERK 1/2 and then incubated with cell lysates after 45 min of cell culture. Phosphorylated states were detected with an anti-phosphotyrosine antibody and normalized to a standard according to the manufacturer's instructions (R&D Systems, DYC1018B).

Immunofluorescence for BMPR and integrin colocalization

Cells were washed with 1× PBS and fixed with 4% formaldehyde solution at 4°C for 15 min. Cells were then permeabilized with a solution of 0.5% Triton X-100 in PBS at 4°C for 5 min. A 1% BSA solution was added, and the cells were incubated at 37°C for 5 min to block nonspecific binding. After blocking, primary antibodies [anti–integrin β_1 (1:50; R&D Systems, MAB17781) and anti-BMPRIa (1:50; Thermo Fisher Scientific, PA5-11856)] were added to the cells and incubated at 37°C for 1 hour. Cells were then washed with 0.5% Tween 20 in PBS (PBST) three times for 5 min each. Thereafter, a biotinylated anti-rabbit secondary antibody (1:50; Vector Laboratories) and a Texas Red anti-mouse secondary antibody (1:50; Vector Laboratories) were added to the cells and incubated at 37°C for 1 hour, followed by 3 × 5% PBST washing. After washing, streptavidin–fluorescein isothiocyanate was added and incubated at 4°C for 30 min. A final 3 × 5% PBST wash was performed, and the nuclei of the cells were stained using Vectashield-DAPI (Vector Laboratories), whereas the samples were mounted on glass slides for fluorescence microscopy.

Smad phosphorylation

Cell lysates (RIPA buffer) were used after culture for 45 min. Proteins (10 μg) were collected per sample. Western blot assays were run in denaturalizing conditions for Smad 1, Smad 1/5, and GAPDH. NuPAGE 4-12% bis-tris gels were purchased from Life Technologies. pSmad antibodies (pSmad 1 and pSmad 1/5) were obtained from Cell Signaling Technology (12656; 1:1000). As a secondary antibody, anti-rabbit IgG antibody (Cell Signaling Technology, 7074; 1:2000) was used. A substrate for sensitive immunodetection system (Life Technologies, Novex) was used before the blot was exposed to x-ray. Protein expression was quantified by image analysis using ImageJ.

In-cell Western assay

Cells were fixed on coverslips using a fixative buffer (10 ml of formaldehyde, 90 ml of 1× PBS, and 2 g of sucrose) at 37°C for 15 min and then permeabilized in cold methanol at 40°C for 5 min. Cells were then blocked in 0.5% blocking buffer (nonfat dry milk powder in

0.1% PBST buffer) at RT for 2 hours followed by 3 × 10-min washing with 0.1% PBST. Cells were then incubated with primary antibodies at 1:200 dilution in blocking buffer at RT for 1.5 hours separately: Smad 1 (Cell Signaling, 6944S), Smad 5 (Cell Signaling, 12534S), pERK 1/2 (Cell Signaling, 4370S), ERK 1/2 (Cell Signaling, 4695S), pFAK (Cell Signaling, 8556p), FAK (Cell Signaling, 13009P), and pRUNX2 (Abgent, AP3559a). After 3 × 10-min washing with 0.1% PBST buffer, cells were incubated with 1:5000 diluted infrared-labeled secondary antibody IRDye 800CW (LI-COR, 926-32211) and 1:2000 diluted CellTag 700 Stain (LI-COR, 926-41090) at RT for 1 hour, followed by 5 × 10-min washing with 0.1% PBST. Glass coverslips were then dried on white paper for infrared signal reading using an Odyssey infrared imaging system.

Immunofluorescence staining for stem cell differentiation

After 14 days of culture, cells were washed in DPBS and fixed with 4% formaldehyde in DPBS at 37°C for 15 min. Afterward, the samples were rinsed in DPBS and a permeabilizing buffer [10.3 g of sucrose, 0.292 g of NaCl, 0.06 g of $MgCl_2$, 0.476 g of Hepes buffer, 0.5 ml of Triton X, in 100 ml of PBS (pH 7.2)] was added at 4°C for 5 min. The samples were then saturated with 1% BSA/DPBS at 37°C for 5 min. Subsequently, they were incubated at 37°C for 1 hour with a primary antibody against osteocalcin (Santa Cruz Biotechnology, sc-73464; 1:50) or osteonectin (Santa Cruz Biotechnology, sc-10758; 1:50) in 1% BSA/DPBS. After washing in PBST, an anti-rabbit secondary antibody (Vector Laboratories; 1:50) was incubated for 1 hour at 37°C. Finally, the samples were rinsed in DPBS before they were mounted in Vectashield containing DAPI staining (Vector Laboratories). A Zeiss fluorescence microscope was used for imaging.

Quantitative real-time PCR

RNA extraction was performed after 14 days of cell culture. Cells were lysed, and total RNA was extracted using a Qiagen RNeasy micro kit (deoxyribonuclease treatment included), and the quantity and integrity of the RNA were measured with NanoDrop (Thermo Fisher Scientific). qPCR was carried out and analyzed to assess the expression of osteocalcin and osteonectin using *GAPDH* to normalize gene expression (a list of the primers used is shown in table S1). Briefly, RNA samples were reverse-transcribed using the QuantiTect Reverse Transcription Kit (Applied Biosystems). qPCR was carried out using the SYBR Select Master Mix (Life Technologies) and the 7500 Real-Time PCR System (Applied Biosystems). *GAPDH* served as the housekeeping gene, and the expression for the genes of interest was normalized to the *GAPDH* expression. Because the SYBR Green method was used, primer sequences for the genes were validated by dissociation curve/melt curve analysis. The comparative cycle threshold method was used for quantification of gene expression. The relative transcript levels were expressed as means ± SD (n = 3 for each group).

Alkaline phosphatase staining

Cells were cultured on materials for 28 days. Noggin (50 ng/ml) was added in a set of samples, and phosphate deposition was analyzed by an alkaline phosphatase assay (Sigma, 86C-1KT). Cells were fixed with the fixative solution (citrate-acetone-formaldehyde solution) at RT for 30 s. Afterward, the samples were stained with the alkaline dye mixture, incubated at RT in the dark for 15 min, counterstained for 2 min with neutral red solution, and rinsed in tap water.

Implant preparation

Polyimide implant tubes presenting holes were coated by solvent casting from solutions of the corresponding synthesized polymers, PEA or PMA, creating a polymer layer on the tube. Implant tubes were dried under vacuum at 60°C to remove solvent traces and were rinsed with Milli-Q water several times before ultraviolet sterilization. FN (Sigma) was adsorbed overnight on the polymer layer from a protein solution (20 μg/ml) in PBS at 37°C. Then, 1% BSA/PBS solution was adsorbed for 30 min at RT to block nonspecific binding sites before the adsorption of the BMP-2 GF (R&D Systems) from a solution (5 μg/ml) in PBS for 1 hour. The adsorption of the proteins was performed by creating a vacuum to force the incoming of the solution into the implant tubes. After each protein adsorption, the samples were rinsed in PBS to remove the nonadsorbed protein and, finally, were kept in PBS until implantation. GFOGER-functionalized PEG-maleimide (PEG-MAL) hydrogels, which have been shown to promote osteogenic differentiation and bone healing of radial segmental defects (*39*), were used as a positive control. Hydrogels were synthesized by reacting the four-arm, MAL–end functionalized (>95%) PEG macromer (PEG-MAL; 20 kD; Laysan Bio) with the adhesive peptide GYGGGPG(GPP)5GFOGER(GPP)5GPC (GFOGER) (Activotec) and BMP-2 (R&D Systems), followed by mixing with VPM cross-linker (AAPTEC) at a volume ratio of 2:1:1:1. The final concentration of the BMP-2 GF in the hydrogels was 75 μg/ml. The concentration of VPM used was calculated to provide the same number of cysteine residues than the number of free (unreacted) MAL groups remaining in the adhesive peptide-functionalized PEG-MAL solution.

Bone radial segmental defect surgery

The Institutional Review Board and the Institutional Animal Care and Use Committee guidelines were followed to perform in vivo experiments. C57B1/6J male mice (8 to 10 weeks old; Jackson Laboratory) were anesthetized under isoflurane, and the right forelimb was shaved and swabbed with isopropyl alcohol and chlorhexidine. After anesthesia induction, mice were provided with a single dose of sustained-release buprenorphine for pain relief. An incision was made in the skin along the forearm, and the muscle tissue over the radius was blunt-dissected. A 2.5-mm defect was created in the center of the radius by using a custom-made double-bladed bone cutter. The implant tube was placed into the defect by fitting it at the proximal and distal ends of the radial defect, and the incision was then closed with degradable vicryl suture. The defect created was checked by the imaging with a radiography system right after the surgery and before the recovery of the animal. Mice were monitored after surgery for signs of distress, movement, and weight loss.

Faxitron and μCT imaging

The radial defects were imaged with the MX-20 Radiography Equipment (Faxitron; 23-kV energy and 15-s scan time) at different time points: 0, 14, 28, 42, and 56 days. For μCT imaging, the length of the radius (3.2 mm) centered on the 2.5-mm radial defect was scanned in anesthetized live mice using a VivaCT system (Scanco Medical; 142-mA intensity, 55-kVp energy, 300-ms integration time, and 15-μm resolution) at 0, 4, and 8 weeks after surgery. Bone formation was evaluated by contouring 2D slices (including only the radius), which were used to obtain 3D μCT reconstructions, displaying the total length of the radius scanned. However, the quantification of the volume of new bone within the defect was performed by evaluating only the middle 2.0 mm of the defect to ensure that only new bone formation was measured.

Histology

At the end of the experiment (8 weeks), mice were euthanized and radial bones were explanted, fixed in 10% neutral-buffered formalin solution, decalcified (decalcifying solution; Ricca), and embedded in paraffin. Sections (5 μm thick) were cut and deparaffinized before the Safranin O/Fast Green staining. Samples were deparaffinized, rehydrated in water, and incubated in Mayer's hematoxylin solution for 10 min. After the samples were rinsed in tap water, they were incubated in 0.5% Fast Green solution for 10 s and rinsed in 1% acetic acid for 3 s. Finally, the samples were incubated in 0.5% Safranin O for 2 min and then dehydrated and cleared in xylene before mounting them using DPX.

Statistical analysis

The Tukey-Kramer method was used with multiple-comparisons posttest ANOVA.

SUPPLEMENTARY MATERIALS

Supplementary material for this article is available at http://advances.sciencemag.org/cgi/content/full/2/8/e1600188/DC1

fig. S1. AFM height (left) and phase (right) images of bare PEA and PMA surfaces at different magnifications from 500 nm to 5 μm.

fig. S2. AFM phase images of BMP-2 and PDGF-BB (100 ng/ml) adsorbed on PEA and PMA, with indication of average size of the GF aggregates on each image.

fig. S3. Colocalization of integrin β_5 and BMPRIa after 1 day of culture on PEA/FN/BMP-2.

fig. S4. Phosphorylation of FAK on PEA using different conditions for BMP-2 presentation: bound on the surface as a coating versus soluble in the culture medium as well as using P5F3 control.

fig. S5. Full longitudinal sections of 8-week radial samples stained with Safranin O/Fast Green.

table S1. Primers for qPCR.

REFERENCES AND NOTES

1. M. M. Martino, P. S. Briquez, K. Maruyama, J. A. Hubbell, Extracellular matrix-inspired growth factor delivery systems for bone regeneration. *Adv. Drug Deliv. Rev.* **94**, 41–52 (2015).
2. P. S. Briquez, J. A. Hubbell, M. M. Martino, Extracellular matrix-inspired growth factor delivery systems for skin wound healing. *Adv. Wound Care* **4**, 479–489 (2015).
3. E. J. Woo, Recombinant human bone morphogenetic protein-2: Adverse events reported to the Manufacturer and User Facility Device Experience database. *Spine J.* **12**, 894–899 (2012).
4. U.S. Food and Drug Administration, *Panel Executive Summary for P050036 Medtronic's AMPLIFY rhBMP-2 Matrix* (FDA, Silver Spring, MD, 2010).
5. D. S. W. Benoit, M. P. Schwartz, A. R. Durney, K. S. Anseth, Small functional groups for controlled differentiation of hydrogel-encapsulated human mesenchymal stem cells. *Nat. Mater.* **7**, 816–823 (2008).
6. O. Chaudhuri, L. Gu, D. Klumpers, M. Darnell, S. A. Bencherif, J. C. Weaver, N. Huebsch, H.-p. Lee, E. Lippens, G. N. Duda, D. J. Mooney, Hydrogels with tunable stress relaxation regulate stem cell fate and activity. *Nat. Mater.* **15**, 326–334 (2015).
7. M. J. Dalby, N. Gadegaard, R. Tare, A. Andar, M. O. Riehle, P. Herzyk, C. D. W. Wilkinson, R. O. C. Oreffo, The control of human mesenchymal cell differentiation using nanoscale symmetry and disorder. *Nat. Mater.* **6**, 997–1003 (2007).
8. A. J. Engler, S. Sen, H. L. Sweeney, D. E. Discher, Matrix elasticity directs stem cell lineage specification. *Cell* **126**, 677–689 (2006).
9. R. J. McMurray, N. Gadegaard, P. M. Tsimbouri, K. V. Burgess, L. E. McNamara, R. Tare, K. Murawski, E. Kingham, R. O. C. Oreffo, M. J. Dalby, Nanoscale surfaces for the long-term maintenance of mesenchymal stem cell phenotype and multipotency. *Nat. Mater.* **10**, 637–644 (2011).
10. B. Trappmann, J. E. Gautrot, J. T. Connelly, D. G. T. Strange, Y. Li, M. L. Oyen, M. A. C. Stuart, H. Boehm, B. Li, V. Vogel, J. P. Spatz, F. M. Watt, W. T. S. Huck, Extracellular-matrix tethering regulates stem-cell fate. *Nat. Mater.* **11**, 642–649 (2012).
11. J. H. Wen, L. G. Vincent, A. Fuhrmann, Y. S. Choi, K. C. Hribar, H. Taylor-Weiner, S. Chen, A. J. Engler, Interplay of matrix stiffness and protein tethering in stem cell differentiation. *Nat. Mater.* **13**, 979–987 (2014).
12. W. L. Murphy, T. C. McDevitt, A. J. Engler, Materials as stem cell regulators. *Nat. Mater.* **13**, 547–557 (2014).
13. M. M. Martino, J. A. Hubbell, The 12th–14th type III repeats of fibronectin function as a highly promiscuous growth factor-binding domain. *FASEB J.* **24**, 4711–4721 (2010).
14. B. G. Keselowsky, D. M. Collard, A. J. Garcia, Surface chemistry modulates fibronectin conformation and directs integrin binding and specificity to control cell adhesion. *J. Biomed. Mater. Res. A* **66**, 247–259 (2003).
15. M. M. Martino, F. Tortelli, M. Mochizuki, S. Traub, D. Ben-David, G. A. Kuhn, R. Müller, E. Livne, S. A. Eming, J. A. Hubbell, Engineering the growth factor microenvironment with fibronectin domains to promote wound and bone tissue healing. *Sci. Transl. Med.* **3**, 100ra189 (2011).
16. M. M. Martino, P. S. Briquez, E. Güç, F. Tortelli, W. W. Kilarski, S. Metzger, J. J. Rice, G. A. Kuhn, R. Müller, M. A. Swartz, J. A. Hubbell, Growth factors engineered for super-affinity to the extracellular matrix enhance tissue healing. *Science* **343**, 885–888 (2014).
17. M. M. Martino, P. S. Briquez, A. Ranga, M. P. Lutolf, J. A. Hubbell, Heparin-binding domain of fibrin(ogen) binds growth factors and promotes tissue repair when incorporated within a synthetic matrix. *Proc. Natl. Acad. Sci. U.S.A.* **110**, 4563–4568 (2013).
18. T. Crouzier, L. Fourel, T. Boudou, C. Albigès-Rizo, C. Picart, Presentation of BMP-2 from a soft biopolymeric film unveils its activity on cell adhesion and migration. *Adv. Mater.* **23**, H111–H118 (2011).
19. G. A. Hudalla, N. A. Kouris, J. T. Koepsel, B. M. Ogle, W. L. Murphy, Harnessing endogenous growth factor activity modulates stem cell behavior. *Integr. Biol.* **3**, 832–842 (2011).
20. D. Suárez-González, K. Barnhart, F. Migneco, C. Flanagan, S. J. Hollister, W. L. Murphy, Controllable mineral coatings on PCL scaffolds as carriers for growth factor release. *Biomaterials* **33**, 713–721 (2012).
21. G. A. Hudalla, W. L. Murphy, Biomaterials that regulate growth factor activity via bioinspired interactions. *Adv. Funct. Mater.* **21**, 1754–1768 (2011).
22. M. Salmeron-Sanchez, P. Rico, D. Moratal, T. T. Lee, J. E. Schwarzbauer, A. J. García, Role of material-driven fibronectin fibrillogenesis in cell differentiation. *Biomaterials* **32**, 2099–2105 (2011).
23. R. Pankov, K. M. Yamada, Fibronectin at a glance. *J. Cell Sci.* **115**, 3861–3863 (2002).
24. P. Kanchanawong, G. Shtengel, A. M. Pasapera, E. B. Ramko, M. W. Davidson, H. F. Hess, C. M. Waterman, Nanoscale architecture of integrin-based cell adhesions. *Nature* **468**, 580–584 (2010).
25. D. Gugutkov, C. González-García, J. C. Rodríguez Hernández, G. Altankov, M. Salmerón-Sánchez, Biological activity of the substrate-induced fibronectin network: Insight into the third dimension through electrospun fibers. *Langmuir* **25**, 10893–10900 (2009).
26. Y. Mao, J. E. Schwarzbauer, Fibronectin fibrillogenesis, a cell-mediated matrix assembly process. *Matrix Biol.* **24**, 389–399 (2005).
27. N. B. Guerra, C. González-García, V. Llopis, J. C. Rodríguez-Hernández, D. Moratal, P. Rico, M. Salmerón-Sánchez, Subtle variations in polymer chemistry modulate substrate stiffness and fibronectin activity. *Soft Matter* **6**, 4748–4755 (2010).
28. D. Gugutkov, G. Altankov, J. C. Rodríguez Hernández, M. Monleón Pradas, M. Salmerón Sánchez, Fibronectin activity on substrates with controlled –OH density. *J. Biomed. Mater. Res. A* **92**, 322–331 (2010).
29. H. Mnatsakanyan, P. Rico, E. Grigoriou, A. M. Candelas, A. Rodrigo-Navarro, M. Salmeron-Sanchez, R. Sabater i Serra, Controlled assembly of fibronectin nanofibrils triggered by random copolymer chemistry. *ACS Appl. Mater. Interfaces* **7**, 18125–18135 (2015).
30. V. Llopis-Hernández, P. Rico, D. Moratal, G. Altankov, M. Salmerón-Sánchez, Role of material-driven fibronectin fibrillogenesis in protein remodeling. *Biores. Open Access* **2**, 364–373 (2013).
31. E. Klotzsch, M. L. Smith, K. E. Kubow, S. Muntwyler, W. C. Little, F. Beyeler, D. Gourdon, B. J. Nelson, V. Vogel, Fibronectin forms the most extensible biological fibers displaying switchable force-exposed cryptic binding sites. *Proc. Natl. Acad. Sci. U.S.A.* **106**, 18267–18272 (2009).
32. J. C. Rodríguez Hernández, M. Salmerón Sánchez, J. M. Soria, J. L. Gómez Ribelles, M. Monleón Pradas, Substrate chemistry-dependent conformations of single laminin molecules on polymer surfaces are revealed by the phase signal of atomic force microscopy. *Biophys. J.* **93**, 202–207 (2007).
33. R. O. Hynes, Integrins: Bidirectional, allosteric signaling machines. *Cell* **110**, 673–687 (2002).
34. M. Phimphilai, Z. Zhao, H. Boules, H. Roca, R. T. Franceschi, BMP signaling is required for RUNX2-dependent induction of the osteoblast phenotype. *J. Bone Miner. Res.* **21**, 637–646 (2006).
35. L. Fu, T. Tang, Y. Miao, S. Zhang, Z. Qu, K. Dai, Stimulation of osteogenic differentiation and inhibition of adipogenic differentiation in bone marrow stromal cells by alendronate via ERK and JNK activation. *Bone* **43**, 40–47 (2008).
36. M. B. Greenblatt, J.-H. Shim, W. Zou, D. Sitara, M. Schweitzer, D. Hu, S. Lotinun, Y. Sano, R. Baron, J. M. Park, S. Arthur, M. Xie, M. D. Schneider, B. Zhai, S. Gygi, R. Davis, L. H. Glimcher, The p38 MAPK pathway is essential for skeletogenesis and bone homeostasis in mice. *J. Clin. Invest.* **120**, 2457–2473 (2010).

37. C. González-García, D. Moratal, R. O. C. Oreffo, M. J. Dalby, M. Salmerón-Sánchez, Surface mobility regulates skeletal stem cell differentiation. *Integr. Biol.* **4**, 531–539 (2012).
38. G. S. Stein, J. B. Lian, A. J. van Wijnen, J. L. Stein, M. Montecino, A. Javed, S. K. Zaidi, D. W. Young, J.-Y. Choi, S. M. Pockwinse, Runx2 control of organization, assembly and activity of the regulatory machinery for skeletal gene expression. *Oncogene* **23**, 4315–4329 (2004).
39. A. Shekaran, J. R. García, A. Y. Clark, T. E. Kavanaugh, A. S. Lin, R. E. Guldberg, A. J. García, Bone regeneration using an alpha 2 beta 1 integrin-specific hydrogel as a BMP-2 delivery vehicle. *Biomaterials* **35**, 5453–5461 (2014).
40. G. Baneyx, L. Baugh, V. Vogel, Coexisting conformations of fibronectin in cell culture imaged using fluorescence resonance energy transfer. *Proc. Natl. Acad. Sci. U.S.A.* **98**, 14464–14468 (2001).
41. B. G. Keselowsky, D. M. Collard, A. J. García, Integrin binding specificity regulates biomaterial surface chemistry effects on cell differentiation. *Proc. Natl. Acad. Sci. U.S.A.* **102**, 5953–5957 (2005).
42. F. M. Watt, B. L. M. Hogan, Out of Eden: Stem cells and their niches. *Science* **287**, 1427–1430 (2000).
43. M. Cantini, P. Rico, D. Moratal, M. Salmerón-Sánchez, Controlled wettability, same chemistry: Biological activity of plasma-polymerized coatings. *Soft Matter* **8**, 5575–5584 (2012).
44. F. A. Vanterpool, M. Cantini, F. P. Seib, M. Salmerón-Sánchez, A material-based platform to modulate fibronectin activity and focal adhesion assembly. *Biores. Open Access* **3**, 286–296 (2014).
45. R. Agarwal, C. González-García, B. Torstrick, R. E. Guldberg, M. Salmerón-Sánchez, A. J. García, Simple coating with fibronectin fragment enhances stainless steel screw osseointegration in healthy and osteoporotic rats. *Biomaterials* **63**, 137–145 (2015).
46. P. M. Comoglio, C. Boccaccio, L. Trusolino, Interactions between growth factor receptors and adhesion molecules: Breaking the rules. *Curr. Opin. Cell Biol.* **15**, 565–571 (2003).
47. L. Fourel, A. Valat, E. Faurobert, R. Guillot, I. Bourrin-Reynard, K. Ren, L. Lafanechère, E. Planus, C. Picart, C. Albiges-Rizo, β3 integrin-mediated spreading induced by matrix-bound BMP-2 controls Smad signaling in a stiffness-independent manner. *J. Cell Biol.* **212**, 693–706 (2016).

Acknowledgments: We acknowledge the advice of A. Clark and J. Garcia (Georgia Institute of Technology) on the in vivo experiments and D. Russell (School of Life Sciences, University of Glasgow) on the histological analysis. **Funding:** This study was supported by the European Research Council (ERC HealInSynergy, 306990), the UK Medical Research Council (MR/L022710/1), the Marie Curie International Outgoing Fellowship program (Protdel 331655), and the NIH (R01 AR062368 and R01 AR062920). **Authors contributions:** V.L.-H., M.C., C.G.-G., Z.A.C., J.Y., and P.M.T. performed the experiments and discussed the results; V.L.-H. prepared the figures; and A.J.G., M.D., and M.S.-S. designed the experiments, discussed the results, and prepared the manuscript. **Competing interests:** The authors declare that they have no competing interests. **Data and materials availability:** All the original data related to this article are within the depository of the University of Glasgow with doi:10.5525/gla.researchdata.311. Additional data related to this paper may be requested from the authors.

Submitted 1 February 2016
Accepted 29 July 2016
Published 26 August 2016
10.1126/sciadv.1600188

Citation: V. Llopis-Hernández, M. Cantini, C. González-García, Z. A. Cheng, J. Yang, P. M Tsimbouri, A. J. García, M. J. Dalby, M. Salmerón-Sánchez,Material-driven fibronectin assembly for high-efficiency presentation of growth factors. *Sci. Adv.* **2**, e1600188 (2016).

Science Advances AAAS

Material-driven fibronectin assembly for high-efficiency presentation of growth factors

Virginia Llopis-Hernández, Marco Cantini, Cristina González-García, Zhe A. Cheng, Jingli Yang, Penelope M Tsimbouri, Andrés J. García, Matthew J. Dalby and Manuel Salmerón-Sánchez (August 26, 2016)

Sci Adv 2016, 2:.

doi: 10.1126/sciadv.1600188

This article is publisher under a Creative Commons license. The specific license under which this article is published is noted on the first page.

For articles published under CC BY licenses, you may freely distribute, adapt, or reuse the article, including for commercial purposes, provided you give proper attribution.

For articles published under CC BY-NC licenses, you may distribute, adapt, or reuse the article for non-commerical purposes. Commercial use requires prior permission from the American Association for the Advancement of Science (AAAS). You may request permission by clicking here.

The following resources related to this article are available online at http://advances.sciencemag.org. (This information is current as of November 10, 2016):

Updated information and services, including high-resolution figures, can be found in the online version of this article at:
http://advances.sciencemag.org/content/2/8/e1600188.full

Supporting Online Material can be found at:
http://advances.sciencemag.org/content/suppl/2016/08/22/2.8.e1600188.DC1

This article **cites 46 articles,** 9 of which you can access for free at:
http://advances.sciencemag.org/content/2/8/e1600188#BIBL

Science Advances (ISSN 2375-2548) publishes new articles weekly. The journal is published by the American Association for the Advancement of Science (AAAS), 1200 New York Avenue NW, Washington, DC 20005. Copyright is held by the Authors unless stated otherwise. AAAS is the exclusive licensee. The title Science Advances is a registered trademark of AAAS

Downloaded from http://advances.sciencemag.org/ on November 10, 2016